© World Scientific Publishing Company DOI: 10.1142/S0219455421500206



A Pyramidal Lattice Frame: Pathways to Inversion

Yue Guan

Department of Mechanical Engineering, Texas Tech University Lubbock, TX 79409, USA yuquan@ttu.edu

Lawrence N. Virgin*

Department of Mechanical Engineering and Materials Science Duke University, Durham, NC 27708, USA l.virgin@duke.edu

> Received 8 May 2020 Accepted 27 September 2020 Published 3 November 2020

This paper considers the load—deflection behavior of a pyramid-like, shallow lattice structure. It consists of four beams that join at a central apex and when subject to a lateral load, it exhibits a propensity to snap-through: a classical buckling phenomenon. Whether this structural inversion occurs, and the routes by which it happens, depends sensitively on geometry. Given the often sudden nature of the instability, the behavior is also examined within a dynamics context. The outcome of numerical simulations are favorably compared with experimental data extracted from the testing of three-dimensional (3D)-printed specimens. The key contributions of this paper are that despite the continuous nature of the physical system, its behavior (transient and equilibria) can be adequately described using a discrete model, and the paper also illustrates the utility of 3D-printing in an accessible research context.

Keywords: Snap-through; buckling; 3D-printing; experimental mechanics.

1. Introduction

The genesis for the material contained in this paper arose from two related but quite distinct prior studies. The first considered shallow geodesic domes. These consisted of structures with a relatively large number of members and joints (in a lattice-like arrangement), with strong symmetry groups^{2,3} related to the overall repetitive triangular/hexagonal form. The second focused on a discrete three degree-of-freedom spring-mass system, in which a control parameter was used to reveal

^{*}Corresponding author.

some interesting equilibrium configurations including bifurcations and transitions, also associated with snap-through type instabilities.^{10–13} These two systems are representative of structures occupying the extremes of the dimensional spectrum: low-order but somewhat abstract in the case of the latter; high-order (continuous) but more realistic in the case of the former. This paper falls between these two: a structure of moderate complexity, continuous, and yet somewhat amenable to relatively low-order (modal) analysis.

Three-dimensional (3D)-printing is proving to be an extremely effective method of producing non-simple geometrical shapes with high precision, and in this paper we make extensive use of this kind of additive manufacturing to produce a number of (slender, elastic) structures suitable for testing under load. ¹⁴ Arch-like structures, when loaded laterally, form a geometry that has a tendency to be relatively effective in terms of stiffness and structural efficiency. 15,16 However, if loaded sufficiently, they also tend to be characterized by a loss of stability associated with a sudden snap-through to an inverted state (if it remains elastic), and although this is sometimes exploited in design it is more typically viewed as an undesirable situation and as such, one to be avoided. It is important to point out that in contrast to previous studies on dome-like structures, 2,7,11,17,18 which have typically consisted of trusslike structures made up of pin-jointed bars, the current structural form is based on individual members that can bend, and local buckling is a possibility depending on geometry (and observed in experiment). However, it will be shown that despite the clearly high-dimensional nature of the systems, the primary behavior can be described in terms of a few dominant modes.

This paper describes the basic geometry of interest, presents equilibrium paths for both finite element (FE) and experimental studies, makes a close examination of the morphing nature of the highly nonlinear underlying potential energy, and finally shows some dynamic trajectories as they meander through the phase space, influenced by various equilibrium points as they go.

2. Background

2.1. The specific form of interest

A shallow pyramidal lattice structure (shown in Fig. 1) is considered in this paper. The structure consists of four nominally identical, slender beam members, connected at the apex with a moment-transmitting joint, i.e. it is frame rather than a (pinjointed) truss, and the central apex lies at a small vertical height relative to the remote perimeter boundaries of the four members, hence, the term pyramid. The members are slender enough to enable local or overall (coupled) buckling behavior. As a result, the structure exhibits non-simple static and dynamical phenomena, behavior that shows a strong connection with the spring-mass systems and geodesic domes mentioned in Sec. 1. Note that though the beam members are designed to be

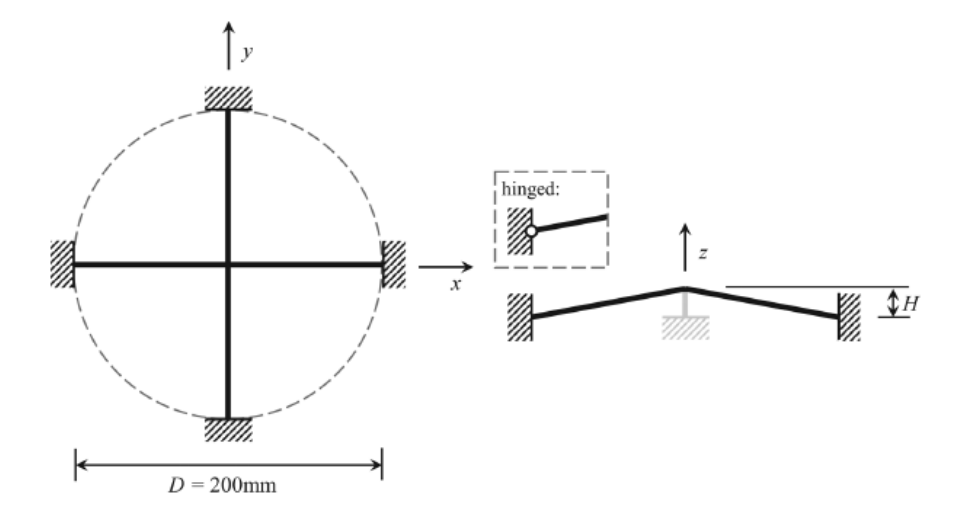


Fig. 1. Geometry of the pyramidal lattice structure.

identical, and the 3D-printing reduces manufacturing error to a minimum, a tiny initial imperfection is still inevitable which will break the symmetry and have a significant influence on the snapping behavior of the frame in experiment.

Rather than focus on a single, specific geometry, we shall present results from a number of frames with related geometries in order to gain a deeper understanding of how geometry influences the key qualitative changes in behavior. Some parameters are fixed, e.g. the location of the boundaries (forming a circle of 200 mm diameter, D), and the use of 3D-printer acrylonitrile butadiene styrene (ABS) thermoplastic. A number of pyramidal structures with various heights, H, cross-sectional areas (always relatively flat in the horizontal direction to promote bending out-of-plane), and boundary conditions, are analyzed and tested. The ratio H/D can be broadly used as a measure of "rise", with nonlinear effects generally increasing with the magnitude of this parameter, despite the relatively shallow geometries considered: in this study we typically consider rises in the range 0.03-0.06. Structure A has "clamped" boundary conditions, meaning that all four members of the structure are rigidly clamped (integrally printed) at the base perimeter. Whereas for structure B, the rotations around the circumference are allowed, turning the boundary conditions into (simply supported) hinges. The number following the structure type represents the height of the structure in millimeters. Table 1 shows a list of the geometric parameters of these structures.

The physical frames were 3D-printed with a Stratasys printer using ABS thermoplastic (with a measured Young's modulus of about 1.9 GPa and a specific gravity very close to unity — note that both of these parameters have some uncertainty associated with them due to the 3D-printing process¹⁹). For structure A, a relatively rigid base perimeter is printed integrally with the frame to provide clamped boundary conditions as shown in Fig. 2(b). Out-of-plane fillets (rounded interior

Table 1. Geometric parameters for the pyramidal lattice structures considered in this study.

Edge fixity	Cross-section (mm)	$I \ (\mathrm{mm^4})$	$\begin{array}{c} \text{Height, } H \\ \text{(mm)} \end{array}$
Clamped	6×2	5.33	6
Clamped	8×2	5.33	8
Clamped	8×2	5.33	10
Clamped	8×2	5.33	12
Hinged	8×1	0.67	12
	Clamped Clamped Clamped Clamped	$\begin{array}{c} \text{(mm)} \\ \text{Clamped} & 6\times 2 \\ \text{Clamped} & 8\times 2 \\ \text{Clamped} & 8\times 2 \\ \text{Clamped} & 8\times 2 \\ \end{array}$	$\begin{array}{cccc} & & & & & & & & \\ & & & & & & & \\ & & & & & & \\ & & & & & \\ & & & & \\ & & & & \\ & & & \\ & & & \\ & & & \\ & & & \\ & & \\ & & \\ & & \\ & & \\ & & \\ & & \\ & & \\ & & \\ & & \\ & & \\ & & \\ & \\ & & \\ $

corners) are used to avoid cracking and stress concentrations. Whereas for hinged boundary conditions, the frame is mounted on low-friction rotating bearings as shown in Fig. 2(a). The central apex joint, however, is still moment transmittable. As a benefit of 3D-printing technology, there is little pre-stress in the structures.

Experimentally, force is applied vertically using a displacement-controlled digital load cell (see Fig. 2(a)). The displacement is measured using three proximity lasers: one to measure the vertical deflection at the apex and the others configured to measure the angle of rotation at the apex in the two orthogonal directions corresponding to the member orientations. To facilitate (amplify) the angular measurements, a lightweight (but relatively rigid) supplementary frame was attached to the apex point as shown in Fig. 2(b). An additional supplementary frame (not shown) was also sometimes used to constrain (clamp) angular deflection, such that purely symmetric behavior could be followed. It is assumed that any material non-linearities are negligible.

2.2. Some numerical details and dimension of the solution space

The structures were analyzed using finite element methods. We shall not emphasize specific aspects, except to say that a code utilizing branch switching was used, in order to follow the anticipated complicated nature of the equilibrium paths and their stability. Branch switching is especially important when tracking equilibrium points emanating from a bifurcation point (e.g. exploiting eigenvector directions). The code used input parameters appropriate to the 3D-printed specimens to provide reasonable correlations with experimentally measured data. Sample runs were verified using ABAQUS. The main approach adopted (reflecting the corresponding experimental approach) for numerical analysis was to apply a point load at the apex and compute the corresponding (static) deflection of the structure, primarily in terms of the three dominant modes of deflection. In addition to static equilibria determination, appropriate inertia effects were included such that an eigenvalue analysis was used to reveal vibrational characteristics including natural frequencies and mode shapes, in order to assess stability.

In general, the overall static and dynamic deformation of the structure can be captured in terms of symmetric (vertical deflection, along the z-axis) and

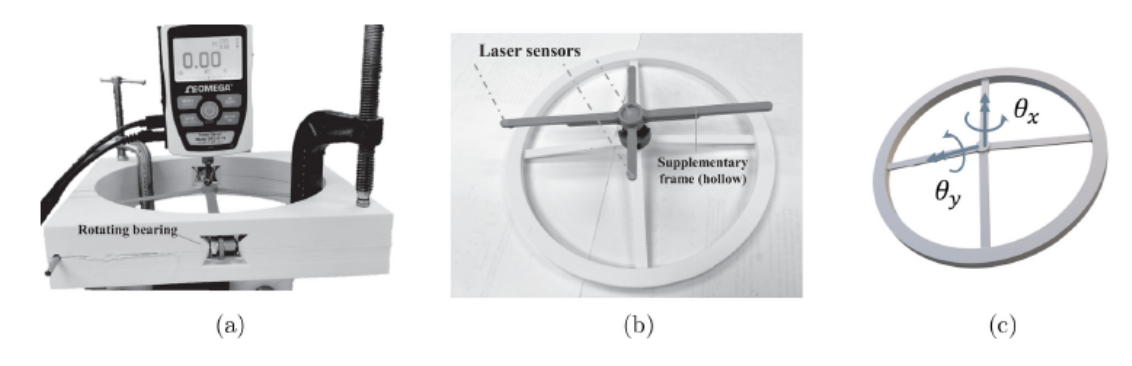


Fig. 2. Experimental images for the frame structures, (a) the frame with vertical load cell applied at the apex, (b) the angle measuring attachment, (c) angles as measured from the apex.

Vibrating modes:

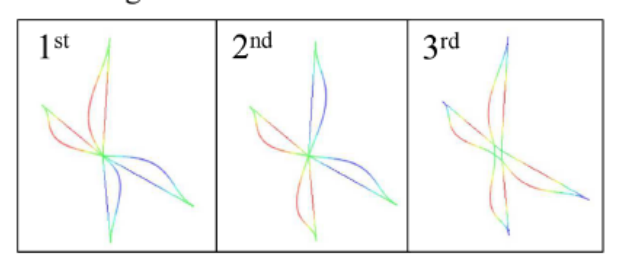


Fig. 3. First three vibrating modes for structure A10.

asymmetric (two rotational angles in the xy-plane at the apex, respectively) shapes, which we can think of as representative modes (see Fig. 3). Under various geometries and boundary conditions, though the order may switch, the first three modes are always well represented by these three displacement components. Without loss of generality, we define the three dominant degrees of freedom (DOF) of the system as Δ (vertical deflection), θ_x and θ_y (rotations about the x- and y-axes). In the FE analysis (FEA) it was concluded that any higher-order behavior (beyond the identified dominant modes) was relatively minor: and we see how this structure can generally be viewed in discrete terms even though strictly speaking it is continuous. It should be mentioned that for other geometries, for example for deeper configurations consisting of more members, the 3D representation may be inadequate.

3. Static Equilibria

Primary interest is focused on equilibrium paths of the structure under the action of a vertical load (P) applied at the apex (in the negative z-direction). Figure 4(a) shows all the numerical and experimental equilibrium paths for structure A8 under the vertical load. The numerical results (solid black lines) are achieved by FEA with arc-length and branch switching methods.^{20,21} The markers represent the experimental results, in which the blue data points show the (free) behavior without any

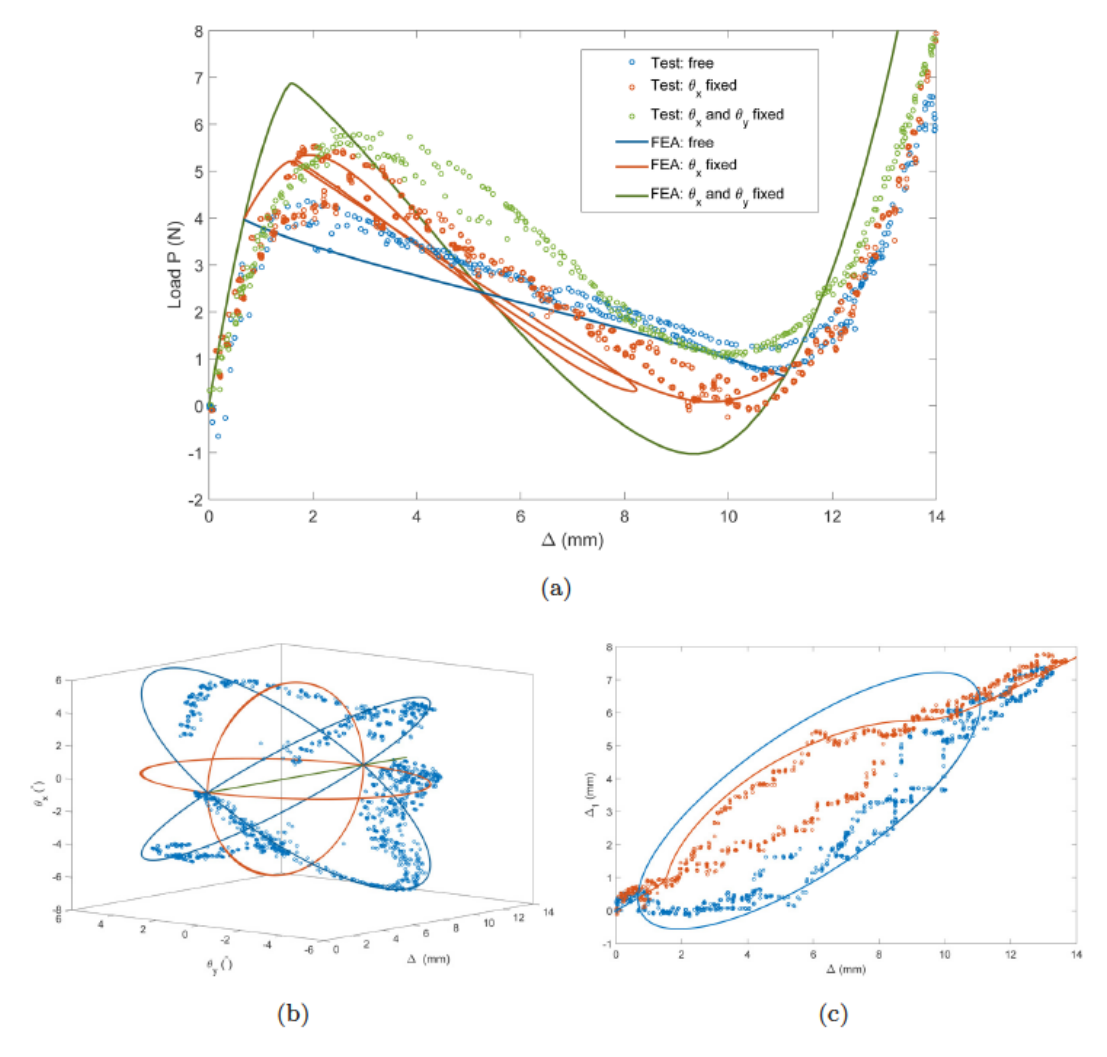


Fig. 4. Equilibrium paths for structure A8: simulation and experimental results, (a) vertical load versus central deflection, (b) deflection versus the two angles, (c) apex deflection versus mid-length deflection.

extra constraints, while the orange and the green data points are test results when one or both of the rotation angles (θ_x and θ_y) are fixed to be zero (using the supplementary frame mentioned earlier). With the help of these extra constraints, the unstable equilibrium paths with symmetric configurations can be observed. The experimental results are consistent with the simulation. However, it is important to appreciate that this load–displacement relationship is just one projection of the equilibrium paths. As shown in Fig. 4(b), in the configuration space, four stable equilibrium paths are actually present — they fall on top of each other in the load-vertical displacement projection, and have configurations as mirror images of each other. All these four equilibrium paths are observed in experiment (shown by blue dots) by perturbing the system manually. There is an inevitable geometric

imperfection in the structure and loading and thus there tends to be a slightly preferred path that is naturally followed. We also take member instability into consideration, with Δ_1 representing the vertical displacement measured at the *middle* point of a beam member. The Δ - Δ_1 relationship should be linear if the member remains unbuckled. However, as can be seen from Fig. 4(c), both the simulation and the experimental results verify the (local) member instability phenomena.

Structure A8 has only one unloaded stable equilibrium (the initial configuration), four index-1 saddles and four index-2 saddles, where the index reflects the degree of instability, i.e. the number of negative eigenvalues from the dynamic analysis. When the height of the structure is increased, more complicated behavior can be generated, a familiar scenario from arch behavior.²² Figure 5 shows the numerical equilibrium paths for structure A10 and all the corresponding "free" equilibrium points (P = 0), and we note the appearance of a stable snapped-through, stable,

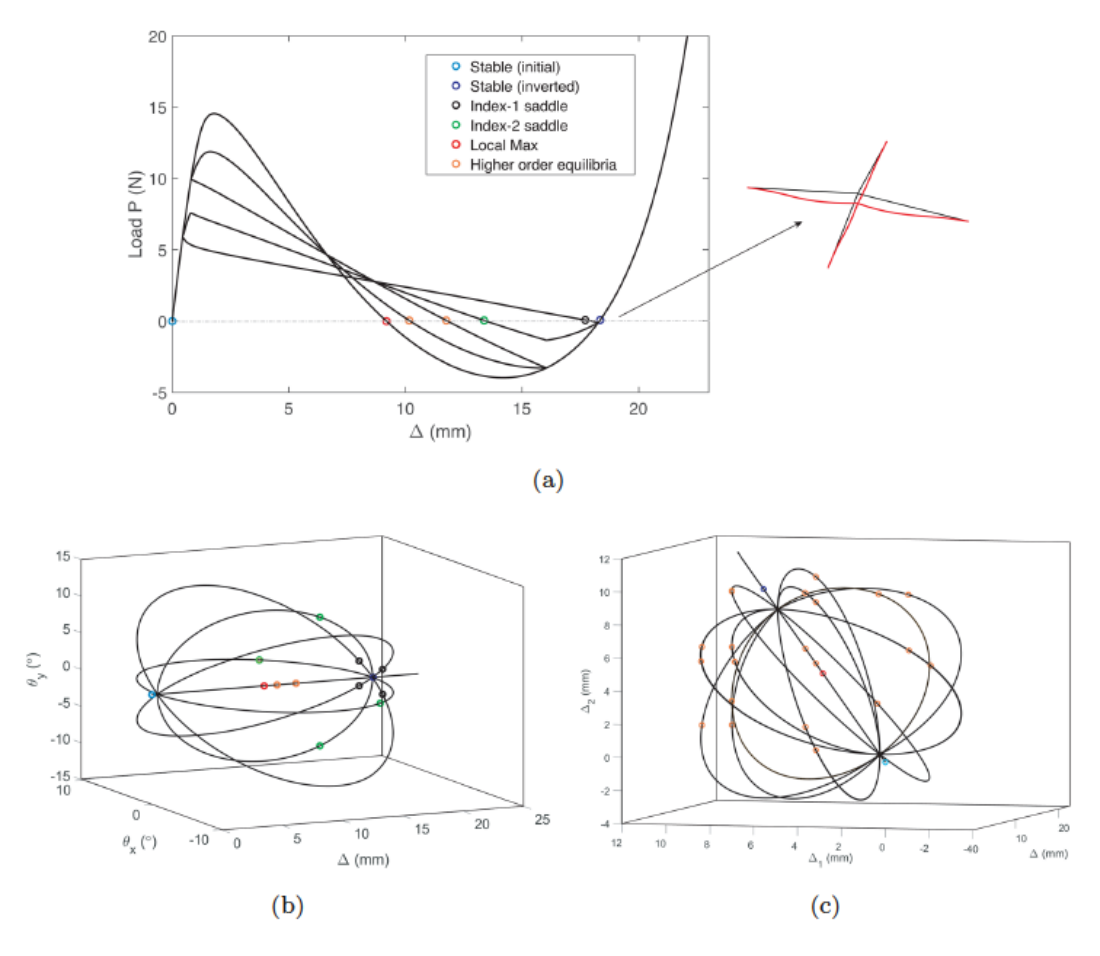


Fig. 5. (a) Numerical equilibrium paths for structure A10 indicating locations of free equilibria (P=0), (b) equilibrium paths in terms of deflection versus the two angles, (c) deflection versus both mid-length deflections.

Table 2. Groups of equilibria (structure A10).

Group	Number of equilibria	Indexa	Color in Fig. 5
1 ^b	1	0	Blue
2	1	0	Blue
3	4	1	Black
4	4	2	Green
5	12	3	Orange
6	8	5	Orange
7	1	7	Red

Notes: ^aThe "index" is the number of unstable eigenvalues. ^bGroup 1 is the initial configuration.

equilibrium configuration (shown in Fig. 5(a)). In total, 31 equilibrium points are obtained, as listed in Table 2. As mentioned earlier, the stability of the equilibria is determined by an eigenvalue analysis in which negative eigenvalues correspond to imaginary natural frequencies. As a result of the symmetry, these equilibria can be divided into seven groups, and again there is a degree of member instability. A number of high-order unstable equilibrium points result from the member buckling phenomenon. After eliminating the influence of these high-order modes, which require a high strain energy level, eleven equilibrium points are exhibited, including two stable points, four index-1 saddles, four index-2 saddles, and one local maximum. The equilibrium paths for structure B12 are qualitatively the same as structure A10, except that the inverted stable point and unstable points are further away from each other. The form and distribution of the equilibrium points are strikingly similar to the parallel mass-spring system mentioned in Sec. 1.9

4. Iso-Potentials

Despite the structures under consideration being continuous, given the dominance of the three dimensions, we can form low-order iso-potential shapes for the pyramidal frames based on FEA, as shown in Fig. 6. Note that the iso-potentials of these pyramidal frames possess very similar characteristics to a real 3-DOF system with analytical governing equations shown in Appendix A. In similarity with a single DOF system, equilibrium is associated with a stationary value of the potential energy, with stability corresponding to a local minimum. In order to reinforce the low-order description we focus on iso-potential shapes based on the lowest potential energy corresponding to the three DOF (Δ , θ_x and θ_y). Here, the self-weight is neglected, and the total potential energy of the system is equal to the strain energy. Under nominally fixed conditions contours of constant potential energy are found. Although this is very familiar for a system with a single DOF, we still have equilibria associated with turning points of the potential energy, but now this requires some care in terms of visualization. Typical results are shown here, and

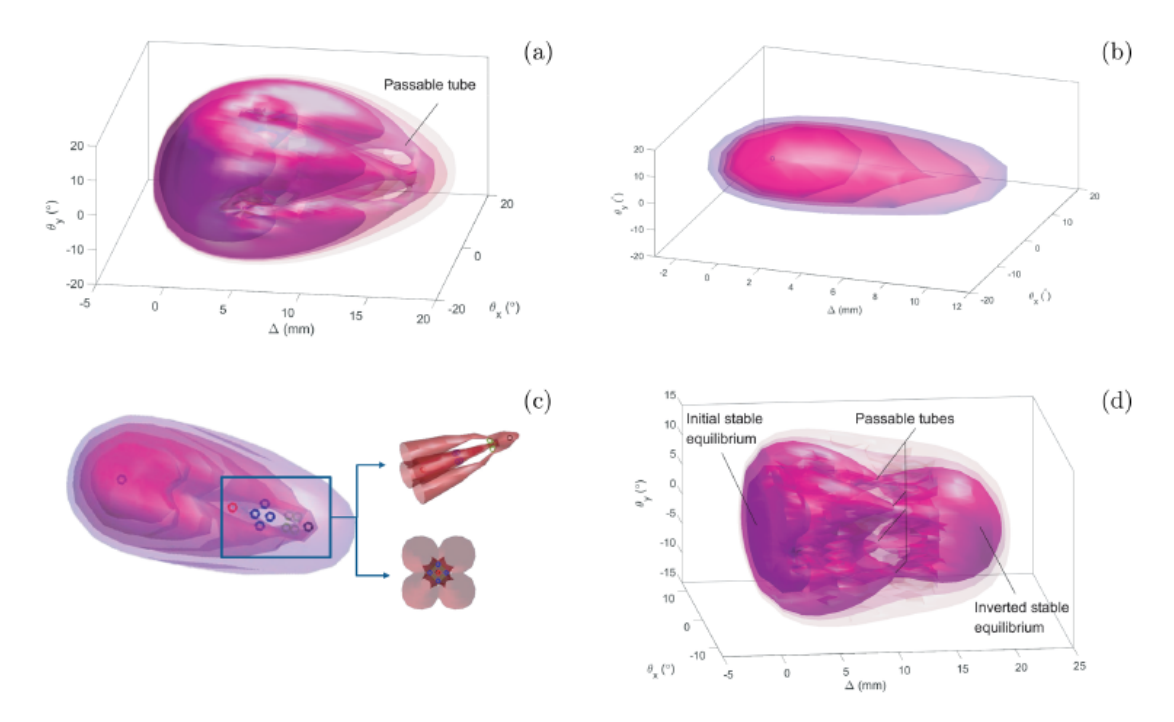


Fig. 6. Iso-potential shapes corresponding to the four geometries, (a) structure A10, (b) structure A6, (c) structure A8, (d) structure B12 (hinged). The shading corresponds to different levels of potential energy, with transparency allowing a visualization of nesting relative to equilibrium points.

later (in Appendix B) we will again appeal to 3D-printing but this time for a physical demonstration of iso-potential shapes.

Four hyperboloid-shaped accessible tubes are found for the frames, whose sectional view is presented in Fig. 6(a) for structure A10. The lack of initial structural symmetry (in Δ), including the disparity of the two stable equilibrium states, is reflected in iso-potential shapes that are significantly asymmetric. The initial equilibrium possesses a relatively low potential energy, and as a result, branches out to a larger stable sphere around it. In contrast, the partially inverted (snapped-through) equilibrium has higher potential energy, lower vibration frequencies (lower eigenvalues), and is in close proximity to the saddle points. All the features reveal that the inverted point is much less stable, that is, less robust against large perturbations. In fact, this equilibrium configuration would disappear for shallower structures, e.g. clamped frames with $H=6\,\mathrm{mm}$, shown in Fig. 6(b) and hence cause the iso-potentials to be single-centered. However, though the remote (partially inverted) stable equilibrium disappears, a "remnant" of the equilibrium still remains in the configuration space, distorting the iso-potential shapes and strongly influencing nearby dynamic trajectories. 23,24

For frames in which the apex is relatively high with regards to the horizontal support plane, the stable sphere around the initial configuration is highly asymmetric, consisting of a round base and four fingers, each pointing to one index-1 saddle point. The four passable tubes, as elongations of the four fingers, would occur under higher potential energy, as well as the inaccessible regions around the local maximum and index-2 saddles. This is shown in Fig. 6(c). However, as the exhibited iso-potential shapes are based on the lowest potential energy corresponding to the three displacements $(\Delta, \theta_x, \theta_y)$, the effects of the fourth and higher vibrating modes cannot be neglected in the vicinity of the local maximum. Therefore, the simplified 3-DOF model might be inadequate under extremely high-energy cases when the transient trajectory approaches the local maximum point. For completeness we also present the iso-potential shapes for the deeper structure (B12) but now the supports are hinged, with a more stable nearly inverted equilibrium configuration as shown in Fig. 6(d).

5. Transient Behavior

In the experiment, three laser sensors are used to measure the vertical deflection, Δ , and the two rotations, θ_x and θ_y , at the apex synchronously, as shown in Fig. 2(a). The differences of the sensor readings, and the distance between them, indicate the two angles at the apex. Structures A10 and B12 are considered in this section. Transient trajectories, in terms of the configuration space, and phase projections in the representative $\Delta - \dot{\Delta}$ plane, are shown in Fig. 7. Arbitrary initial disturbances (in position and velocity) were used to generate transient trajectories, some of which were sufficiently high energy to cause a snap-through response. The sampling rate of the lasers allowed an accurate measurement of velocity. The stable equilibria can be located intuitively. Although the unstable equilibria "screen" can be observed from the phase projection (from a general slowing down), it is difficult to distinguish these unstable equilibrium points in the configuration pace. For clarity, a few typical transient trajectories are extracted and presented in Fig. 8 for both structures, with equilibrium points superimposed. The saddle points appear to attract and then repel all adjacent transient trajectories (at least for these relatively high-energy initial conditions, started close to the initial equilibrium configuration). Adjacent trajectory divergence is found in the vicinity of index-1 and index-2 saddles. The phenomena are especially remarkable for structure B12, in which all saddle points constitute an invisible barrier, determining the snap-through possibilities for the trajectories.²⁵ Furthermore, because of the small magnitude of the negative eigenvalue at the index-1 saddles and relatively low damping, the trajectories are able to oscillate around the index-1 saddles for a few cycles before veering away. In terms of the underlying potential energy, a long mild-gradient sphere occurs in the vicinity of the saddle points, and this promotes a temporary oscillation in the stable directions around these unstable equilibria.^{24,26}

Figure 9 shows a representative projection of the theoretical iso-potential shape for structure A10, with a typical experimental trajectory meandering around it

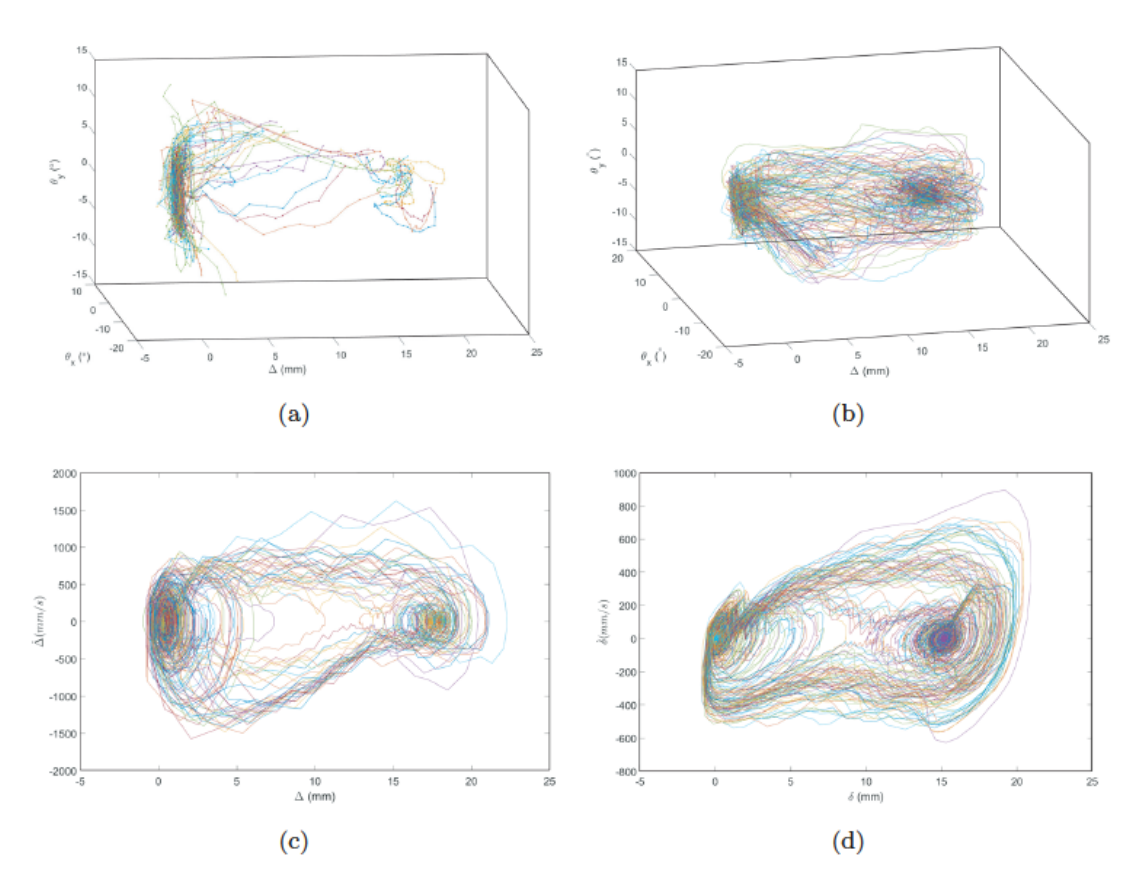


Fig. 7. Transient trajectories, (a) structure A10 configuration space, (b) structure B12 configuration space, (c) structure A10 phase projection, (d) structure B12 phase projection.

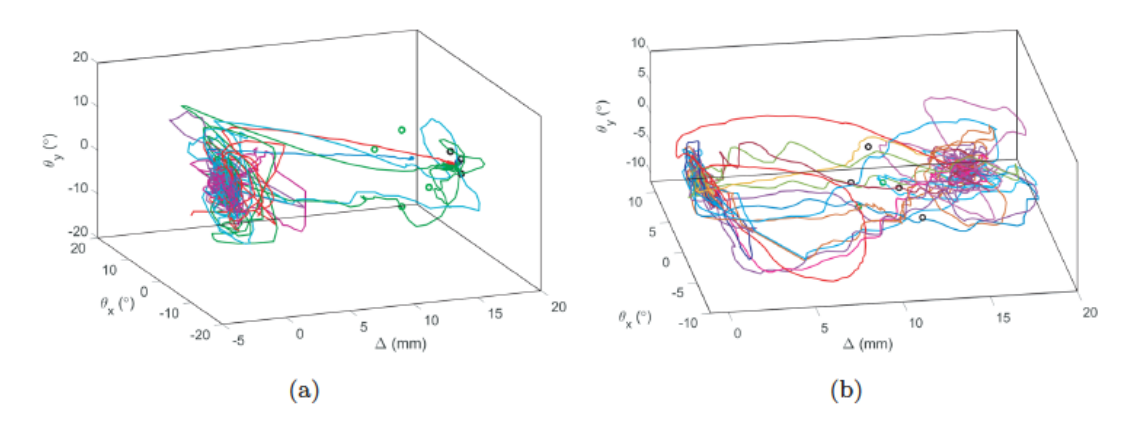


Fig. 8. Some specific transient trajectories superimposed on the equilibrium points, (a) structure A10, (b) structure B12.

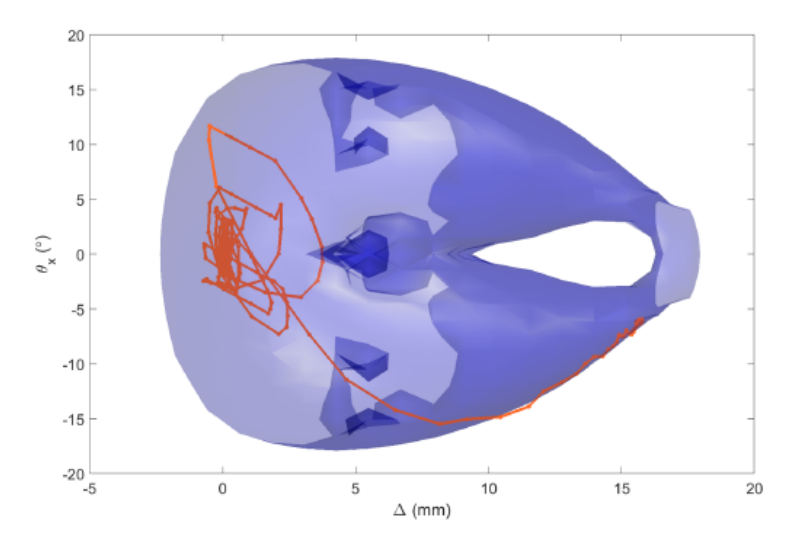


Fig. 9. A transient trajectory moving along an iso-potential (structure A10).

before finally ending up back at the initial equilibrium configuration. Although difficult to observe in a projected view, it is interesting to observe the trajectory avoiding regions of high energy. It is possible for trajectories to snap-through and stay on the inverted (remote) stable equilibrium, but this much less likely given the relative sizes of the basins of attraction: a crucial difference between local and global stability.²⁷

6. Conclusion

Pyramidal lattices are representative of a group of structures in which the behavior under loading is often characterized by highly nonlinear equilibrium configurations with the possibility of snap buckling in which part or the whole of the structure may invert. This is most readily observed when the load is applied quasi-statically. Bifurcations occur, including a typical transition from (axi)-symmetric to asymmetric deformation, and this depends sensitively on the geometry of the initial configuration, especially the rise. Even under quasi-static loading the instability is often manifest as a sudden, discontinuous jump in the response: the system snapsthrough. When the load is applied suddenly, dynamic trajectories are generated and the evolution of these are heavily influenced by the equilibria of the underlying structure, especially unstable equilibria (saddle points) that are not usually available in an experimental context. Potential energy is a useful tool in assessing the overall environment in which the behavior develops. Although this approach has often been used in the context of a single DOF, and sometimes 2-DOF, the specific geometric forms considered in this paper allow a 3-DOF view, an opportunity for 3D-printing, in addition to the exploitation of 3D-printing for the structures themselves. And this provides insight into the daunting nature of highly nonlinear behavior in high-dimensional systems.

Acknowledgments

This work was partially supported by the NSF under award number CMMI-1926672. We are grateful to a reviewer for helpful suggestions.

Appendix A. Comparison With a Discrete 3-DOF Spring-Mass System

In this appendix, a real 3-DOF spring-mass system with very similar behavior and iso-potential shapes to the pyramidal frame is introduced. As shown in Fig. A.1(a), the system is composed of three masses and a single spring. The masses are connected to each other by rigid bars with negligible weights. The 3-DOF of the system are defined as the three clockwise rotation angles θ_1 , θ_2 and θ_3 . Here, we present the governing equations (Eq. (A.1)) and iso-potential shapes (Fig. A.1(b)) of this system without derivation. Further studies on this 3-DOF system can be seen in Ref. 9.

$$(m_{1} + m_{2} + m_{3})R_{1}^{2}\dot{\theta}_{1}^{2} + m_{2}R_{1}R_{2}\dot{\theta}_{2}\cos(\theta_{1} - \theta_{2}) + m_{3}R_{1}R_{3}\dot{\theta}_{3}\cos(\theta_{1} - \theta_{3})$$

$$+ 2m_{2}R_{1}R_{2}\dot{\theta}_{2}^{2}\sin(\theta_{1} - \theta_{2}) + 2m_{3}R_{1}R_{3}\dot{\theta}_{3}^{2}\sin(\theta_{1} - \theta_{3})$$

$$- m_{2}R_{1}R_{2}\dot{\theta}_{1}\dot{\theta}_{2}\sin(\theta_{1} - \theta_{2}) - m_{3}R_{1}R_{3}\dot{\theta}_{1}\dot{\theta}_{3}\sin(\theta_{1} - \theta_{3})$$

$$- (m_{1} + m_{2} + m_{3})gR_{1}\sin\theta_{1} + k_{1}R_{1}\left[X_{0}\cos\theta_{1} - Y_{0}\sin\theta_{1} + R_{2}\sin(\theta_{1} - \theta_{2})\right]$$

$$\cdot \left[L_{01} - (\Delta_{x1}^{2} + \Delta_{y1}^{2})^{1/2}\right](\Delta_{x1}^{2} + \Delta_{y1}^{2})^{-1/2}$$

$$+ k_{2}R_{1}\left[X_{0}\cos\theta_{1} - Y_{0}\sin\theta_{1} + R_{3}\sin(\theta_{1} - \theta_{3})\right]$$

$$\cdot \left[L_{02} - (\Delta_{x2}^{2} + \Delta_{y2}^{2})^{1/2}\right](\Delta_{x2}^{2} + \Delta_{y2}^{2})^{-1/2} = 0,$$

$$m_{1}R_{1}R_{2}\dot{\theta}_{1}\cos(\theta_{1} - \theta_{2}) + m_{2}R_{2}^{2}\dot{\theta}_{2}$$

$$- 2m_{2}R_{1}R_{2}\dot{\theta}_{1}^{2}\sin(\theta_{1} - \theta_{2}) + m_{2}R_{1}R_{2}\dot{\theta}_{1}\dot{\theta}_{2}\sin(\theta_{1} - \theta_{2}) - m_{2}gR_{2}\sin\theta_{2}$$

$$+ k_{1}R_{2}\left[Y_{0}\sin\theta_{2} - X_{0}\cos\theta_{2} + R_{1}\sin(\theta_{1} - \theta_{2})\right]$$

$$\cdot \left[L_{01} - (\Delta_{x1}^{2} + \Delta_{y1}^{2})^{1/2}\right](\Delta_{x1}^{2} + \Delta_{y1}^{2})^{-1/2} = 0,$$

$$m_{1}R_{1}R_{3}\ddot{\theta}_{1}\cos(\theta_{1} - \theta_{3}) + m_{3}R_{3}^{2}\ddot{\theta}_{3}$$

$$- 2m_{3}R_{1}R_{3}\dot{\theta}_{1}^{2}\sin(\theta_{1} - \theta_{3}) + m_{3}R_{1}R_{3}\dot{\theta}_{1}\dot{\theta}_{3}\sin(\theta_{1} - \theta_{3}) - m_{3}gR_{3}\sin\theta_{3}$$

$$+ k_{2}R_{3}\left[Y_{0}\sin\theta_{3} - X_{0}\cos\theta_{3} + R_{1}\sin(\theta_{1} - \theta_{3})\right]$$

$$\cdot \left[L_{02} - (\Delta_{x2}^{2} + \Delta_{y2}^{2})^{1/2}\right](\Delta_{x2}^{2} + \Delta_{y2}^{2})^{-1/2} = 0,$$
(A.1)

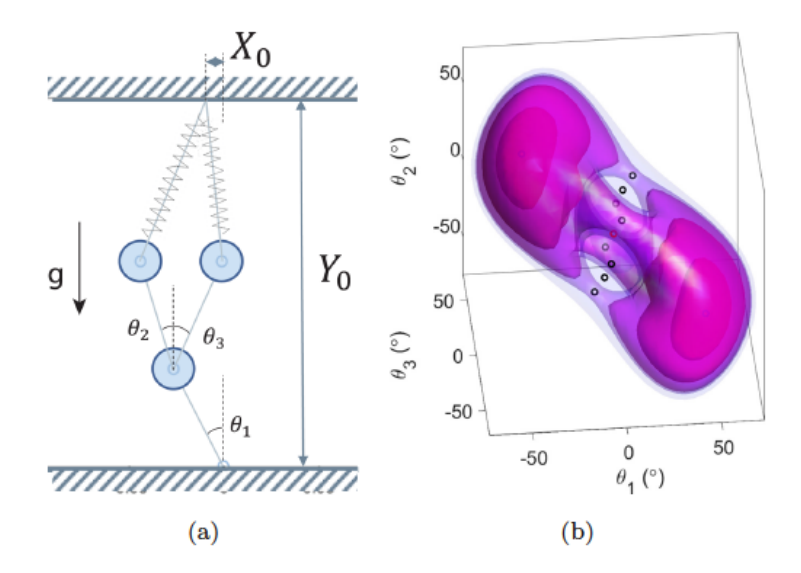


Fig. A.1. A 3-DOF spring-mass system, (a) schematic, (b) iso-potential shapes.

where

$$\Delta_{x1} = R_1 \sin \theta_1 + R_2 \sin \theta_2 - X_0,$$

$$\Delta_{y1} = R_1 \cos \theta_1 + R_2 \cos \theta_2 - Y_0,$$

$$\Delta_{x2} = R_1 \sin \theta_1 + R_3 \sin \theta_3 - X_0,$$

$$\Delta_{y2} = R_1 \cos \theta_1 + R_3 \cos \theta_3 - Y_0.$$

In the above equations, m_1 , m_2 and m_3 denote the masses of the three weights, and R_1 , R_2 and R_3 are the radius of the rotating rigid bars. As can be seen, the iso-potentials for the 3-DOF system based on the above governing equations exhibit similar shapes as pyramidal frame, including two stable equilibria and four hyperboloid-shaped accessible tubes around the index-1 saddles. The behavior of the three dominant DOF in the pyramidal frame $(\Delta, \theta_x \text{ and } \theta_y)$ can be related to the behavior of θ_1 , θ_2 and θ_3 in this spring-mass system, respectively. And the influence of the rise (H) of the of the pyramidal frame is somewhat equivalent to the influence of Y_0 shown in Eq. (A.1).

Appendix B. 3D-Printed Iso-Potentials

In this appendix, we present some 3D-printed renditions of iso-potentials. The grey object in Fig. B.1(a) corresponds to structure A10 and thus is equivalent to Fig. 6(a) (and Fig. 9), similarly with the orange shape (structure B12) and Fig. 6(b). Figures B.1(b) and B.1(c) shows the two co-existing stable equilibrium configurations: the initial shape in part (b), and the snapped-through configuration in part (c). Despite the necessarily limited resolution of the 3D-printing technique, we view the

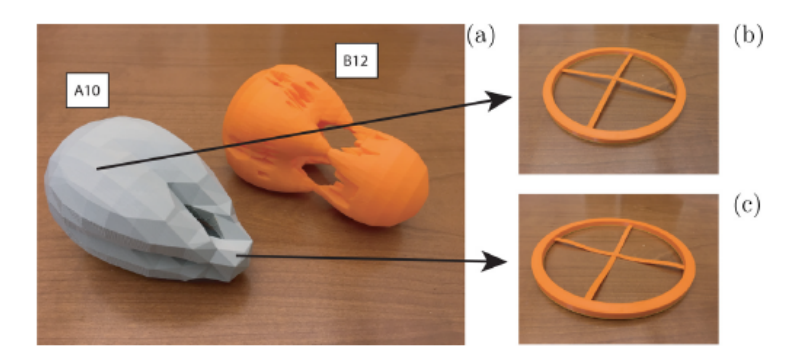


Fig. B.1. (a) Some 3D-printed renditions of iso-potentials, (b) and (c) equilibrium shapes corresponding to structure A10.

snapping between these shapes as trajectories passing through the tubes connecting the bulbs surrounding the stable equilibria, and passing close to (and influenced by) the saddle-points that separate them. At rest in an initial equilibrium configuration, snap-through occurs given either sufficient applied force in a quasi-static sense, or sufficient initial velocity (kinetic energy) to generate large transient trajectories, provided a remote (inverted) equilibrium configuration is available.

References

- Y. Guan, L. N. Virgin and D. Helm, Structural behavior of shallow geodesic lattice domes, Int. J. Solids Struct. 155 (2018) 225–239.
- T. J. Healey, A group-theoretic approach to computational bifurcation problems with symmetry, Comput. Methods Appl. Mech. Eng. 67(3) (1988) 257–295.
- A. Kaveh and M. Nikbakht, Stability analysis of hyper symmetric skeletal structures using group theory, Acta Mech. 200(3-4) (2008) 177-197.
- C. H. Coan and R. H. Plaut, Dynamic stability of a lattice dome, Earthq. Eng. Struct. Dyn. 11 (1983) 269–274.
- X. Chen and S. Z. Shen, Complete load-deflection response and initial imperfection analysis of single-layer lattice dome, Int. J. Space Struct. 8 (1993) 271–278.
- V. Gioncu, Buckling of reticulated shells: State-of-the-art, Int. J. Space Struct. 10 (1995) 1–46.
- K. Abedi and G. A. R. Parke, Experimental study of dynamic propagation of local snap-through in single-layer braced domes, Int. J. Space Struct. 16(2) (2001) 125–136.
- R. H. Plaut, Snap-through of shallow reticulated domes under unilateral displacement control, Int. J. Solids Struct. 148–149 (2018) 24–34.
- 9. Y. Guan and L. N. Virgin, Stability and bifurcation in discrete mechanical systems: An experimental and analytical study, *Int. J. Bifurcation Chaos* **30** (2020) 2030024.
- C. S. Hsu, Equilibrium configurations of a shallow arch of arbitrary shape and their dynamic stability character, Int. J. Non-Linear Mech. 3(2) (1968) 113–136.
- H. Rothert, T. Dickel and D. Renner, Snap-through buckling of reticulated space trusses, J. Struct. Div. 107 (1981) 129–143.
- I. M. Kani and R. E. McConnel, Collapse of shallow lattice domes, J. Struct. Eng. 113 (1987) 1806–1819.

- Z. Chen, Q. Guo, C. Majidi, W. Chen, D. J. Srolovitz and M. P. Haataja, Nonlinear geometric effects in mechanical bistable morphing structures, *Phys. Rev. Lett.* 109(11) (2012) 114302.
- T. Chen, J. Mueller and K. Shea, Integrated design and simulation of tunable, multistate structures fabricated monolithically with multi-material 3D printing, Sci. Rep. 7 (2017) 1–8.
- Y. C. Fung and A. Kaplan, Buckling of low arches or curved beams of small curvature, Technical report, NACA Technical Note 2840 (1952).
- P. S. Harvey and L. N. Virgin, Coexisting equilibria and stability of a shallow arch: Unilateral displacement-control experiments and theory, Int. J. Solids Struct. 54 (2015) 1–11.
- 17. K. Murota and K. Ikeda, Computational use of group theory in bifurcation analysis of symmetric structures, SIAM J. Sci. Stat. Comput. 12(2) (1991) 273–297.
- K. Koohestani and A. Kaveh, Efficient buckling and free vibration analysis of cyclically repeated space truss structures, Finite Elem. Anal. Des. 46(10) (2010) 943–948.
- L. N. Virgin, On the flexural stiffness of 3D printer thermoplastic, Int. J. Mech. Eng. Educ. 45(1) (2017) 59–75.
- S. Ligarò and P. Valvo, A self-adaptive strategy for uniformly accurate tracing of the equilibrium paths of elastic reticulated structures, Int. J. Numer. Methods Eng. 46 (1999) 783–804.
- 21. K. K. Choong and E. Ramm, Simulation of buckling process of shells by using the finite element method, *Thin-Walled Struct.* **31**(1–3) (2002) 39–72.
- 22. L. N. Virgin, Y. Guan and R. H. Plaut, On the geometric conditions for multiple stable equilibria in clamped arches, *Int. J. Non-Linear Mech.* **92** (2017) 8–14.
- S. T. Trickey and L. N. Virgin, Bottlenecking phenomena near a saddle-node remnant in a Duffing oscillator, Phys. Lett. A 248 (1998) 185–190.
- 24. R. Wiebe and L. N. Virgin, On the experimental identification of unstable static equilibria, *Proc. R. Soc. A*, *Math. Phys. Eng. Sci.* 472(2190) (2016) 1–15.
- E. E. Zotos, A Hamiltonian system of three degrees of freedom with eight channels of escape: The great escape, Nonlinear Dyn. 76(2) (2014) 1301–1326.
- Y. Xu and L. N. Virgin, Probing the force field to identify potential energy, J. Appl. Mech. 86 (2019) 101008.
- L. N. Virgin, Introduction to Experimental Nonlinear Dynamics (Cambridge University Press, 2000).